From Waste to Wealth: A Cellulose-based Fibrous Membrane from Recycled Cigarettes Supported with Dual Perovskite for Formaldehyde Degradation at Room Temperature

Anyang Duan
Jiangnan University
Tian Wang
Jiangnan University
Shuanglin Wu
Jiangnan University
Chenhao Ji
Jiangnan University
Qiyao Ma
Jiangnan University
Fenglin Huang (flhuang@jiangnan.edu.cn)
Jiangnan University

Research Article

Keywords: formaldehyde removal, cellulose acetate, recycled cigarettes, electrospinning, double perovskite

Posted Date: September 13th, 2022

DOI: https://doi.org/10.21203/rs.3.rs-2039644/v1

Additional Declarations: No competing interests reported.

Version of Record: A version of this preprint was published at Cellulose on May 12th, 2023. See the published version at https://doi.org/10.1007/s10570-023-05251-3.

Abstract

Formaldehyde, as a hazardous indoor contaminant following house decoration, is essential to its efficient removal at room temperature. This paper reports an eco-friendly approach for extracting cellulose acetate (CA) from waste cigarette filters to construct a nanofibrous composite membrane for formaldehyde degradation at ambient temperature. A composite nanofibrous membrane was fabricated by salable electrospinning of cellulose acetate and La2CoMnO6/CeO2(LC), followed by hydrolysis and potassium doping with KOH. The membrane demonstrates excellent catalytic activity (97.56 % of conversion), super stability (95.35 % of conversion after 50 h) and long service life (93.96 % of conversion after 3 catalysis cycles), which is ascribed to the synergistic catalytic effect of double perovskite and rapid hygroscopic properties of cellulose. In addition, the obtained membrane has a higher moisture regain (7.82 %) than that of the LC/CA nanofibrous membrane (2.21 %), and higher than that of the commercial air filter membrane using polypropylene (PP) fiber (near zero), accelerating formaldehyde adsorption and fastening the water removal, thereby allowing for the long-term positive progress of formaldehyde catalytic oxidation reaction. This work provides encouraging guidance for further exploration into formaldehyde degradation, which is promising for application in air cleaning.

1 Introduction

With the increasing decoration industry, indoor building materials and coatings have released a large amount of volatile organic compound gases (VOCs), such as formaldehyde, toluene, xylene, etc (Liang et al., 2018). Formaldehyde (HCHO) has been globally recognized as the most abundant and most toxic of harmful gases indoors. Studies have shown that long-term living in an environment with excessive formaldehyde content can lead to many serious diseases, such as pneumonia, emphysema and even cancer (Tang et al., 2009). Hence, the efficient elimination of indoor HCHO is urgently desired at ambient temperature.

Common methods of HCHO removal are adsorption, photocatalytic and thermos catalysis, which have limited adsorption capacity, high energy consumption and low efficiency (Bellat et al., 2015; Li et al., 2014; Liu et al., 2018). The ambient condition catalytic oxidation method has advantages with high catalytic efficiency, is environmentally friendly and energy-saving, so it has been studied extensively (Ye et al., 2020). With metal oxides as the primary catalysts for the removal of HCHO to date, it has been challenging to obtain high efficiency at ambient temperatures (Guo et al., 2023). Although many scientists doped metal oxides with precious metals to improve the catalytic activity at room temperature, the cost is increased significantly (Freyschlag and Madix, 2011).

Recently, perovskites are believed as the most promising catalyst for efficient HCHO removal at room temperature due to their low price, good catalytic activity and controllable structure (Morales et al., 2014; Wang et al., 2019; Yang et al., 2022). For example, researchers (Huang et al., 2016) fabricated a $Co_xMn_{3-x}O_4$ nanosheet array on carbon fiber fabric for HCHO removal. The results shows that the as-synthesized catalytic material could completely convert formaldehyde into carbon dioxide and water at temperatures below 80°C. It is also found that the catalytic oxidation performance of perovskites depended on the number of active sites and oxygen mobility (Xu et al., 2021). What's more, through adjustment of the morphology, crystal plane structure, size or doping of perovskite, its active site could be regulated, which further competently built oxygen vacancies and increase the number of reactive oxygen species, thereby improving the catalytic efficiency at room temperature (Ding et al., 2022; Liu et al., 2022; Wang et al., 2019).

Because traditional powder catalysts are prone to loss during their applications, usually, powder catalysts are immobilized on suitable supports with more uniform dispersion, better catalytic performance and better mechanical property (Phan et al., 2018; Zhou et al., 2022).

Tang et al (Tang et al., 2006). reported that the catalytic activity of MnO_x-CeO_2 for HCHO in dry air is higher than that in humid air, because water covers the active sites and prevents the adsorption of HCHO gases. However, the catalytic longevity of HCHO oxidation is prolonged in humid air, because water is decomposed into hydroxyl groups, which could

effectively promote the forward progress of the catalytic reaction. Therefore, the cellulose-based membrane is considered a promising catalyst carrier due to its outstanding hydrophilic property and an abundance of hydroxyl groups. Our group (Wu et al., 2022; Huang et al., 2015) extracted the pure cellulose acetate from discarded cigarette filters, and successfully prepared a cellulose membrane for lithium batteries by electrospinning. The waste cellulose acetate cigarette filters have non-biodegradability and toxicity, posing a serious threat to the ecological environment. Thus, retrieving a cellulose acetate cigarette filter and using it as a catalyst carrier could turn waste into wealth, which is beneficial to relieve environmental contamination and economize resources. In order to evenly disperse the catalyst on the support, the nanofibrous membrane generation by electrospinning is considered as ideal option due to its large specific surface area and high porosity (Mai et al., 2022; Zhang et al., 2022). Moreover, an expanded fabrication method has rarely been reported, and hunting for a scalable strategy plays an important role in practical application.

In this study, cellulose acetate derived from waste cigarette filters was scalable electrospun with the LC dual perovskite to prepare composite nanofibrous membrane. The hydrophilicity, catalytic activity and stability are further enhanced by converting cellulose acetate to cellulose and doping potassium via KOH hydrolysis. The above obtained the optimal membrane could achieve a formaldehyde conversion of 97.56% at 20 ℃, which only dropped to 95.35% after 50 h and without any change after three cycles. Additionally, according to the formaldehyde catalytic oxidation, a reaction mechanism is proposed, including the key roles of potassium doping and cellulose in the reaction. This paper provides an environmentally friendly, cost-effective, and excellent catalytic performance cellulose composite with a dual perovskite nanofibrous membrane, which give an important inspiration for the research on the catalytic oxidation performance of formaldehyde at room temperature.

2 Experimental

2.1 Materials

Lanthanum nitrate hexahydrate ($La(NO_3)_3·6H_2O$) was provided by Beijing Enokai Technology Co., Ltd, China. 50% manganese nitrate (50% $Mn(NO_3)_2$), Cobalt nitrate hexahydrate ($Co(NO_3)_2·6H_2O$), Cerium nitrate hexahydrate ($Ce(NO_3)_3·6H_2O$), ammonium carbonate ($(NH_4)_2CO_3$), potassium hydroxide (KOH) and 40% formalin were provided by Sinopharm Chemical Reagent Co. LTD, China. Dimethylacetamide (DMAc) and acetone were provided by Sinopharm Chemical Reagent Co., Ltd, China. All chemical reagents used above are analytical ones. The commercial PP air filter membrane was purchased from Celgard Corporation, USA. All the chemicals were directly used without further purification. Various brands of waste cigarette filter were collected from the used cigarette butts in daily life.

2.2 Syntheses of catalysts

La_2CoMnO_6/CeO_2 nanoparticles (NPs) were synthesized by the precipitation method. After $La(NO_3)_3·6H_2O$, 50% $Mn(NO_3)_2$, $Co(NO_3)_2·6H_2O$ and $Ce(NO_3)_3·6H_2O$ were dissolved in deionized water with the stoichiometric ratio, the aqueous solution of $(NH_4)_2CO_3$ (1 mol/L) was added dropwise with vigorous stirring until pH value was 9. The suspension was then aged for 6 h at ambient temperature. The precipitate was filtrated out and washed with deionized water until the pH of the filtrate was approximately 7. The sample was fully dried at 100°C and calcined at 900°C for 3 h in the air. The obtained catalyst was denoted as LC. Alkali metal-doped La_2CoMnO_6 was prepared through the co-impregnation of La_2CoMnO_6 with aqueous KOH (1 mol/L). After the catalyst was washed with ethanol for several times, it was completely dried at 100°C. This obtained catalyst was denoted as K-LC.

2.3 Preparation of cigarette filter membrane

Firstly, the collected waste cigarette filter was consisted of wrapper, residual tobacco ash and cellulose acetate, which was soaked in deionized water for 12 h and then cleaned with ethanol under ultrasonication (UP400S ultrasonicator) for several time to remove impurities. The cleaned filters were dried at 60 ℃ in vacuum. After that, the cleaned waste cigarette filters

(CA, 15%) and LC NPs with different concentrations (1%, 2%, 3%, 4%) were dissolved in a mixed solvent of n, n-dimethylacetamide (DMAc) and acetone (2:3) with vigorous stirring for 12 h to obtain the electrospinning solution. Subsequently, all cigarette filter membrane was fabricated through scalable electrospinning and then dried at 60°C. The obtained samples were denoted as 1% LC/CA, 2% LC/CA, 3% LC/CA and 4% LC/CA. The above as-prepared membranes were hydrolyzed in 0.1 mol/L of KOH solution for 24 h. After the nanofibrous membrane was washed with ethanol for several times, and dried at 60°C. The obtained samples were denoted as 1% K-LC/C, 2% K-LC/C, 3% K-LC/C and 4% K-LC/C.

2.4 Characterizations

The morphology of samples was characterized on a scanning electron microscope (SEM, JEOL SU8010, Hitachi) with an energy dispersive X-ray spectrum (EDS). Transmission electron microscopy (TEM, Hitachi) and high-resolution transmission electron microscopy (HRTEM, Hitachi) were performed using a JEOL JEM-2100 instrument at an accelerating voltage of 200 kV. The crystal structures of samples were characterized on an X-ray diffraction (XRD) (D2 PHASER, BRUKER AXS, Germany) with a Cu Kα radiation (= 1.5406 Å) over Bragg angles from 5 ° to 80 ° and a scanning speed of 10 ° min^{-1}. The catalyst size and fiber diameter were measured by Ps and Nano Measure 1.2 software, respectively. Moisture regain of membrane was measured using an international standard ISO139:2005. The N_2 adsorption-desorption isotherm was tested by Brunauer–Emmett–Teller (BET) method on a TriStar-II 3020 surface area (Micromeritics, Micromeritics Instrument Corp., USA). Fourier transform infrared spectra (FTIR) spectra were collected using a TFS Nicolet iS10 FTIR spectrophotometer (Thermo Fisher Scientific, USA) in the wavenumber range of 500 cm^{-1} to 4000 cm^{-1}. X-ray photoelectron spectroscopy (XPS) was performed on a Thermo Scientific K-Alpha+ (Thermo Fisher Scientific, USA). The binding energy values were all calibrated based on the hydrocarbon contamination using the C1s peak at 284.8 eV, and surface element contents were calculated through XPS peak areas. H_2 temperature-programmed reduction (H_2-TPR) was performed on an AutoChem1 II 2920 (Micromeritics, USA).

2.5 Catalytic activity evaluation

The catalytic oxidation of HCHO was evaluated in a fixed-bed quartz tube reactor (Φ4 mm) with 0.1 g catalyst (40 − 60 mesh). HCHO gas was generated through the evaporation of formalin solution (40%, Aldrich) at 140°C, which was brought into the reaction tube through 21% O_2 in N_2. The gas flow rate was adjusted and controlled with a mass flow controller. HCHO and CO_2 were analyzed on a Multi-Gas Analyzer (GC-2030AF, Shimadzu Corporation, Japan). The HCHO catalytic oxidation testing of the nanofibrous membrane took place in a self-assembled air simulation reactor with a volume of 1 m^3. The 40% formalin solution was dropped into a beaker on the left of the reactor, which was completely volatilized with a heater (NBW-946M) at 140 ℃ to prepare formaldehyde gas. The initial concentration of formaldehyde in the reactor was controlled by adjusting the volume of formalin added. The concentration of HCHO and CO_2 was measured with respective detector (AM7p and SW-723). The nanofibrous membrane was fixed on the square hole of the separator in the middle of the reactor, and the fan was installed on the left side of the reactor to form an air circulation.

A gas mixture with a GHSV of 60000 $mL{\cdot}g^{-1}{\cdot}h^{-1}$, 200 ppm of HCHO, and 64% air humidity was fed into the reactor. The dependence of HCHO removal and adsorption efficiency with various sample on temperature was studied at a temperature range of 0–80°C. The effect of HCHO initial concentration (200 ppm, 400 ppm, 600 ppm) on HCHO conversion was researched at 20 ℃. Change of the HCHO conversion overtime was discussed at 20 ℃ for 52 h. The catalytic material's stability was investigated at 20°C for 72 hours. The HCHO adsorption was calculated and HCHO conversion was obtained according to the following Eqs. (1) and (2).

$$\mathrm{HCHOadsorption} = \frac{[\mathrm{HCHO}]_{\mathrm{out}}}{[\mathrm{HCHO}]_{\mathrm{in}}} \times 100\%$$

1

$$\mathrm{HCHO conversion} = \frac{[\mathrm{CO_2}]_{\mathrm{out}}}{[\mathrm{HCHO}]_{\mathrm{in}}} \times 100\%$$

2

where, $[HCHO]_{in}$, $[HCHO]_{out}$ and $[CO_2]_{out}$ are the initial, final HCHO concentration of the flow gas and the CO_2 concentration in the products, respectively.

3 Results And Discussion

3.1 Scalable production of the catalytic materials

Figure 1 provides a scalable fabrication process of the K-LC/C composite nanofibrous membrane and schematic illustration of its application for formaldehyde purification. First, an extensive LC/CA membrane was fabricated with LC nanoparticles (NPs) and recycled cellulose acetate from cigarette filters by a controllable electrospinning equipment. The electrospun LC/CA membrane was then hydrolyzed by KOH, and the resulting membrane was termed K-LC/C. The ester bond on each cellulose acetate glucose unit ring is broken under alkaline conditions, resulting in the formation of additional hydroxyl groups (Olaru et al., 2001). The acetic acid reacts rapidly with potassium hydroxide to create potassium acetate, which ionizes CH_3COO^-. The obtained K-LC/C membrane possesses more abundant hydroxyl and higher moisture absorption than that of LC/CA membrane, enabling it to effectively removes moisture and advances the HCHO catalytic oxidation reaction. Furthermore, the double perovskite has a regular cube structure and abundant metal ions with strong oxidizing, as displayed in the schematic, which demonstrates its structural controllability and promising catalytic activity. Especially, CeO_2 contains plentiful oxygen vacancies according its structure, which presents prosperous oxygen evolution and oxygen storage capabilities. Following that, the catalyst's metal-oxygen bonds become easier break due to doped potassium during hydrolysis process, resulting in an abundance of oxygen defects. Accordingly, the oxidation capability of double perovskite is obviously strengthened, and it could efficiently decompose formaldehyde. Subsequently, the catalytic activity of all nanofibrous membrane was evaluated in a closed self-assembly simulation reactor.

3.2 Characterization of the catalytic materials

Figure 2a-c shows the SEM, TEM and HRTEM images of LC NPs, respectively. As shown in Fig. 2a, LC NPs has a nearly spherical or short rod-like structure with a smooth surface, and its size ranges from 23 to 45 nm. The van der waals force between nanoparticles is stronger than that of its self-gravity, resulting in agglomeration slightly. (Ma et al., 2022). As shown in Fig. 2b, the darker portion is considered as La_2CoMnO_6 because of its heavy metal, and CeO_2 displays the light-colored could be observed in the LC NPs. The HRTEM image of LC NPs (Fig. 2c) illustrates that there are two different kinds of lattice fringes. The fringe interval of 0.23 nm is matched the interplanar spacing of the (200) plane in La_2CoMnO_6, while stripe spacing of 0.31 nm could be assigned to the (111) crystallographic plane of CeO_2. (Bu et al., 2020; Li et al., 2016).

Figure 2d collects the XRD patterns of La_2CoMnO_6, LC and K-LC NPs. According to XRD patterns (Fig. 3c), LC NPs has obvious diffraction peaks at 22 °, 32 °, 40 ° and 47 °, which are consistent with the diffraction peaks of La_2CoMnO_6(Silva et al., 2016). Meanwhile, CeO_2 diffraction peaks are detected with no extra peaks in LC NPs (PDF #34–0394), indicating that LC NPs is successfully synthesized. Compared to LC NPs, K-LC NPs has similar peaks with attenuated peak intensity, suggesting that the incorporation of potassium might lead to the decrease in size and crystallinity of LC NPs (López-Suárez et al., 2014). The analysis of the TEM, HRTEM and XRD indicates that CeO_2 is successfully supported on the La_2CoMnO_6.

The EDS-mapping (Fig. 2e) and pattern (Fig. 2f) of K-LC NPs illustrate five peaks for lanthanum (La), cobalt (Co), manganese (Mn), cerium (Ce) and potassium (K) with weight% of 36.78%, 18.63%, 15.8%, 14.23% and 14.56%, respectively. It's not hard to evidenced that potassium has been anchored onto the LC NPs, and the weight proportions of La, Co, Mn and

Ce elements are consistent with their stoichiometric ratio. It could be conclusion that K-LC NPs has been synthesized successfully by XRD and EDS results.

Figure 3a shows TEM images of LC/CA nanofibrous membrane with different catalyst concentration. It could be observed that LC NPs is respectively distributed on the surface and interior of nanofibers. There are less catalysts supported on the nanofibers when loading concentration is less than three percent, resulting in limited catalytic activity. However, LC NPs enters the interior of nanofibers with serious agglomeration in 4% LC/CA, which decreases catalyst's utilization. All in all, LC NPs is the most uniformly dispersed and extensively extended on the nanofiber surface in the 3% LC/CA nanofibers. The LC NPs floating on the surface of the nanofiber further enhance its specific surface area and catalytic activity. Figure 3b-i depicts SEM images and fiber diameter distribution images of different nanofibrous membrane. As shown in Fig. 3b, c and Fig. 3f, g, the CA nanofibers exhibits uniform shape and fineness with an average diameter of 143.21 nm, while both cellulose nanofibers have rough surfaces and uneven fineness with an average diameter of 165.74 nm. The roughed surface of the nanofiber could increase the specific surface area and active sites, which is conducive to the adsorption and oxidation of formaldehyde. From Fig. 3d, e and Fig. 3h, i, the diameter of K-LC/C nanofibers (177.27 nm) become thicker than that of LC/CA (152.37 nm), the results are consistent with the above. The reason is that the penetrated interior of cellulose acetate by KOH could destroy the hydrogen bonding force between cellulose acetate chains and dissolve its crystalline region partially, which assigned to rough surface.

Figure 3j, k investigates the FTIR spectra and moisture absorption curve of various nanofibrous membrane. As shown in Fig. 3j, peaks at 1743 cm^{-1}, 1230 cm^{-1}, 1370 cm^{-1} and 3700 – 3200 cm^{-1} are due to the stretching vibration of C = O, the stretching vibration of the acetyl ester bond, the deformation vibration of -CH_3 and the stretching vibrations of OH, respectively (Zhang et al., 2018, Naragund and Panda, 2020). After the alkaline hydrolysis of CA and LC/CA membrane, peaks of C = O, -CH_3 and acetyl ester bonds almost disappear in cellulose and K-LC/C, while the intensity peak of OH is enhanced due to the generation of new hydroxyl groups. All results indicates that the CA and LC/CA are reduced successfully to cellulose and K-LC/C membrane. As shown in Fig. 3k, all as-prepared membrane's moisture return is further superior than the commercial PP air filter fiber membrane (near zero). It is obvious that the moisture regain in K-LC/C (7.82%) and cellulose (7.65%) is preferable than that of LC/CA (2.21%) and CA (2.18%) membrane. From the beginning of the curve, the moisture adsorption speed over the K-LC/C and cellulose is significantly faster than CA and LC/CA membrane. Moreover, it could be observed that the catalyst loading has hardly any effect on the hygroscopicity of the membrane. On the basis of the above FTIR and moisture regain analysis, it could be concluded that the excellent hygroscopic properties of the K-LC/C membrane could be attributed to a multitude of hydrophilic groups. The existence of hydrophilic groups is not only conducive to the transfer of water, but also to promote the adsorption of formaldehyde, which is a prerequisite for the efficient oxidation of formaldehyde.

Figure 4a-e gives the N_2 adsorption-desorption isotherm and the corresponding pore size distribution curves of different nanofibrous membrane. It could be classified as the typical IV isotherms with hysteresis loops according to IUPAC classification, illustrating that their pore sizes are spread from micro- to mesopores (Liu et al., 2017; Qu et al., 2018). By calculating the N_2 adsorption-desorption isotherms, the surface area of cellulose nanofibrous membrane (7.8 $m^2 \cdot g^{-1}$) is the highest compared with other membrane. The membrane's surface area would decrease with increased concentration due to catalyst agglomeration. However, the surface area of 3% K-LC/C membrane (5.4 $m^2 \cdot g^{-1}$) is higher than that of 2% K-LC/C (5.0 $m^2 \cdot g^{-1}$) and 4% K-LC/C (2.8 $m^2 \cdot g^{-1}$), which could be attributed to more catalyst NPs distributed in the nanofiber's surface rather than gathered in interior. This is consistent with the SEM analysis. Moreover, the pore size distribution of all the samples displays a double pore size of around 2.8 nm and 4.7 nm, which is consistent with the above analysis. Thence, these conclusions supported the micro-mesoporous structure of the cellulose or a series of K-LC/C nanofibrous membrane.

Figure 4f explores the commercial PP, CA and cellulose membrane for HCHO adsorption property. The commercial PP membrane shows the lowest formaldehyde adsorption efficiency of 13.23%, which attributes to smaller surface area (3.8 $m^2 \cdot g^{-1}$). The surface area of CA nanofibrous membrane (8.3 $m^2 \cdot g^{-1}$) is larger than that of cellulose membrane, however, the formaldehyde adsorption efficiency of cellulose membrane (36.52%) is much higher than that of CA membrane (21.23%). Theoretically, the hydroxyl groups are easily connected with hydrogen bonds in formaldehyde through intermolecular hydrogen bonds, which is beneficial to adsorbing formaldehyde (He et al., 2022; Liu et al., 2020). Thus, it could be reasonable that improvement of formaldehyde adsorption efficiency in cellulose membrane attributed to its increased hydroxyl groups. In general, electrospun cellulose nanofibrous membrane could be an ideal support for a catalyst that gets rid of formaldehyde.

3.3 Catalytic activity for HCHO removal

Figure 5a shows the catalytic activity of LC and K-LC NPs for HCHO elimination at different temperature. LC itself is largely inactive at room temperature, although 89.22% of HCHO conversion is obtained at 20°C. The K-LC NPs, 98.71% of HCHO conversion is obtained at 20°C, indicating that the added potassium might promote the catalytic activity of LC, especially at room temperature. The catalytic activity of the LC/CA and K-LC/C nanofibrous membrane series in the HCHO oxidation at various temperatures is shown in Fig. 5b, c. Obviously, at a catalyst concentration range of 1–4%, the K-LC/C membrane reactivity is much higher than LC/CA in the formaldehyde removal, which is attributed to potassium doping and superior hygroscopicity. The 3% K-LC/C membrane shows the preferably activity, affording nearly 97.56% of HCHO conversion at 20°C. Typically, with a higher catalyst concentration supported, a higher formaldehyde conversion could be achieved. However, 4% K-LC/C only have 86.51% of HCHO conversion at 20 ℃, which is lower than that of 2% K-LC/C, probably because the catalyst concentration is too high and lead to agglomeration inside the nanofibers, which further blocks the pores of the nanofiber membrane, and result in a decrease in available active sites of supported catalyst(Zhao et al., 2021). Meanwhile, decomposing 1 mol HCHO can generate 1 mol H_2O, meaning that the decomposition of 200 ppm HCHO can produce 149 mg of water. Results shows that the 3% K-LC/C after the formaldehyde oxidation is 51 mg heavier than before. which indicated that 3% K-LC/C have an excellent hygroscopicity, and H_2O is partially decomposed into hydroxyl due to the potassium doping(Bai and Li, 2014; Ji et al., 2020). Figure 5d shows the effect of 3% K-LC/C membrane on HCHO conversion with different initial concentration. It could be indicated that HCHO conversion on the 3% K-LC/C membrane decrease with an increase in reaction concentration. The HCHO conversion at 200 ppm presents the highest catalytic activity, which is attributed to the sufficient active site and is beneficial to the reaction between membrane and HCHO. In general, these conclusions indicates that the 3% K-LC/C have high catalytic activity.

Figure 5e tests the change of HCHO conversion over time at 20 ℃. The conversion of HCHO is 97.56% and 87.88% initially and remains above 95.35% and 86.71% within 50 h over the K-LC/C and LC/CA membrane, which have excellent stability. In contrast, the K-LC and LC NPs shows relatively poor stability. The HCHO conversion of K-LC NPs decreases from 98.71–83.23%. The conversion of HCHO is dropped from 89.23–76.53% in LC NPs. It could be concluded that the cellulose and CA membrane could endow the granular catalyst with excellent sustained release properties and improve the recyclability of the catalyst. What's more, the cellulose membrane not only act as a carrier, but also make a significant contribution to the catalytic activity and the continuation of the catalytic reaction due to its excellent hygroscopic properties and abundant hydroxyl groups. Figure 5f demonstrates the catalytic stability and regeneration activity with different sample at 20 ℃. The results indicates that the HCHO conversion is severely decrease after three cycles for K-LC and LC NPs. Fortunately, 3% K-LC/C and 3% LC/CA membrane have excellent catalytic stability during 72 h test. In particular, the HCHO conversation of 3% K-LC/C is maintained nearly at 97.56% even after three regenerations, suggesting its great potential in indoor application for air cleaning.

3.4 Reaction mechanism of HCHO oxidation

Table 1
Relative Concentration Ratios of Mn, Co, Ce and O

catalysts	O_{ada}/O	O_{surf}/O	O_{latt}/O	Co^{3+}/Co	Co^{3+}/Co^{2+}	Mn^{4+}/Mn	Mn^{4+}/Mn^{3+}	Ce^{4+}/Ce	Ce^{4+}/Ce^{3+}
LC	12.94%	42.26%	45.70%	35.24%	0.88	43.32%	1.98	53.42%	3.84
K-LC	14.71%	62.71%	22.58%	45.36%	1.19	52.11%	2.53	65.32%	5.92

Fig. 6a-d approves the relative atomic concentration ratios and element chemical valence state on the La_2CoMnO_6, LC and K-LC catalyst surfaces by XPS results. As shown in Fig. 6a, the Co 2p spectra is separated into two distinct peaks corresponded to Co^{2+} (780.8 eV) and Co^{3+}(779.7 eV), respectively (Zhang et al., 2014). As shown in Fig. 6b, Mn 2p spectra are fitted into two deconvoluted peaks at 644.1 and 642.0 eV ascribed to Mn^{4+} and Mn^{3+} peaks, respectively (Mathew et al., 2012). From table 1, the relative atomic concentration ratios of Co^{3+}/Co or Mn^{4+}/Mn over the LC NPs (35.24 % or 43.32 %) is much less than that of K-LC NPs (45.36 % or 53.42 %). It is interesting that many more Co^{3+} or Mn^{4+}species exist on the surface of the K-LC NPs. It has been certificated that the Co^{3+} or Mn^{4+} species could be preferable for the high activity in the HCHO removal reaction. As shown in Fig. 6c, Ce 3d XPS spectra of the LC and K-LC illustrates eight peaks associated with spin-orbit doublet pairs. Labeled as u(u-u‴) and v(v-v‴) are related to the 3d3/2 and 3d5/2 spin-orbit components, respectively. The couple (u', v') are characteristic peaks of Ce^{3+} species and the remaining peaks are ascribed to Ce^{4+} species in CeO_2(Cwele et al., 2016). It is clear that Ce^{4+}/Ce values (53.42 %) for LC are lower than K-LC NPs (65.32 %). It is generally recognized that the more Ce^{4+} species are beneficial for redox properties over the Ce-based catalysts, resulting in an enhancement of catalytic activity. As shown in Fig. 6d, the O 1s spectrum is deconvoluted into three peaks attributed to the lattice oxygen at 529.7-530.3 eV, the surface activated oxygen at 530.7-531.6 eV and the adsorbed oxygen species (O^{2-}, O_{2-}, O^-) at 532.7-532.9 eV, denoted as O_{latt}, O_{surf} and O_{ads}, respectively(Jia et al., 2016). According to the relative concentration ratios of O in **table 1**, the O_{surf}/O and O_{ads}/O value on the K-LC are much higher than those of the LC, but the O_{latt}/O value is gradually decreasing. This could be attributed to part of the O_{latt} is converted to O_{surf} , which causes an abundance of active site induced by potassium doping. It is demonstrated that more O_{ads} and O_{surf} species could be facilitated to the oxidation of HCHO into CO_2.

Fig. 6e evaluates the reducibility of LC and K-LC NPs by H_2-TPR. As shown in Fig. 6e, LC NPs displays three H_2 consumption peaks at 340.6 ℃, 417.5 ℃ and 602.8 ℃, attributed to $Mn^{4+}\rightarrow Mn^{3+}$, $Ce^{4+}\rightarrow Ce^{3+}$ and $Co^{3+}\rightarrow Co^{2+}\rightarrow Co^0$ (Zhang et al., 2014). For K-LC NPs, the H_2-TPR exhibits three peaks around 257.9 ℃, 402.2 ℃, 581.3 ℃. By comparison, all the reduction peaks of K-LC NPs shift in a lower direction, presenting better reduction performance than LC NPs. The low-temperature reduction peaks at 257.9 ℃, indicating that O_{surf} and O_{ads} are restored on K-LC NPs simultaneously (Meng et al., 2018). It is reasonable to deduce that the metal-oxygen bond is easier to break due to potassium doping, generating additional O_{ads} to promote redox properties over K-LC NPs.

According to above XPS and H_2-TPR analysis, **Fig. 6f** proposes a probable mechanism for enhanced HCHO decomposition over K-LC/C membrane. Typically, HCHO is first adsorbed on the K-LC/C nanofibrous membrane, which is then oxidized by strong oxidizing metal ions (Mn^{4+}, Mn^{3+}, Co^{3+}, or Ce^{4+}). Meanwhile, high valence metal ions are reduced to low-valent metal ions (Mn^{3+}, Mn^{2+}, Co^{2+}, or Ce^{3+}) with the generation of oxygen vacancies. These generated oxygen vacancies are supplemented by the migration of oxygen in the air and bulk lattice oxygen, follow by generating in reactive oxygen species (O^{2-}, O_{2-}, or O^-). The doped potassium is favor for the formation of oxygen vacancies. This reason is that the electron density is transferred from the K valence band to the Co d band, increasing the Pauli repulsion between Co and O (Ji et al., 2020; Zhang et al., 2014). Whereafter, the low-valence metal ions are converted high-valence through strongly oxidizing reactive oxygen species, which form the redox cycle to ensure high catalytic activity. Research has shown that the product water will cover the oxygen vacancies during the catalytic oxidation reaction (Mathew et al., 2012). The K-LC/C membrane

with superior hygroscopicity is not only rapidly absorb moisture but also promote the decomposition of water into hydroxyl groups. This reason is that K has strong electronegativity, a low work function and a large surface dipole moment compared with C and H, which tends to interact with O in H_2O through a directly bond (Cwele et al., 2016). These as-generated hydroxyl groups promote the formaldehyde with a rapid decomposition into formate and carbonate intermediates as shown in the following equations. In addition, HCHO adsorption is enhanced by hydroxyl groups in the K-LC/C membrane through its hydrogen bonding with formaldehyde (Bai and Li, 2014).

4 Conclusions

In summary, waste cigarette filters as raw materials were utilized to produce cellulose acetate, and composited with La_2CoMnO_6/CeO_2 by a scalable electrospinning method. After alkaline hydrolysis, the waste cigarette filters were converted to cellulose to prepare the K-LC/C nanofibrous membrane. The K-LC/C nanofibrous membrane demonstrates good moisture absorption and enhanced formaldehyde adsorption. The K-LC/C membrane exhibits super catalytic activity, high stability and better cycling compared to the LC/CA membrane. Especially, 3% K-LC/C membrane presents 97.56% of conversion for HCHO elimination at 20 ℃, which is only decreased to 95.35% after 50 h and 93.96% even after three repetitive catalyst generation cycles. This could be attributed to its enhanced hygroscopic and increased active adsorption sites. Furthermore, after the doping of potassium into perovskite NPs, an abundant hydroxyl group can be generated and significantly promote the removal of indoor formaldehyde at room temperature over perovskites. Consequently, the as-prepared nanofibrous membrane could be a viable candidate for treating HCHO pollution and lowering cigarette filter pollution for the environment.

Declarations

Ethics approval and consent to participate

This article does not contain any studies with human participants or animals performed by any of the authors.

Consent for publication

The manuscript is approved by all authors for publication. I would like to declare on behalf of my co-authors that the work described was original research that has not been published previously, and not under consideration for publication elsewhere, in whole or in part. All the authors listed have approved the manuscript that is enclosed.

Availability of data and materials

The data that support the findings of this study are available from the corresponding author upon reasonable request.

Declaration of competing Interest

The authors declare that they have no known competing financial interests or personal relationships that could have appeared to influence the work reported in this paper.

Funding

This work was supported by the Jiangsu Key R&D Program (BE2017060, BE2016707), and the 111 Project (B17021).

Authors' contributions

A.D. designed and performed the experiment, and wrote the manuscript. T.W. analyzed the data and revised the manuscript. S.W. offered suggestions for the experiments. and C.J. offered suggestions for the characterizations of materials. Q.M. revised the manuscript. F.H. critically revised and gave the final approval for the article, and is the corresponding author.

Acknowledgments

The authors gratefully acknowledge the Jiangsu Key R&D Program (BE2017060, BE2016707), and the 111 Project (B17021).

Authors' information

Anyang Duan[a], Tian Wang[a], Shuanglin Wu[a], Chenhao Ji[a], Qiyao Ma[a], Fenglin Huang*[a]

[a] Key Laboratory of Eco-textiles, Ministry of Education, Jiangnan University, Wuxi, Jiangsu 214122, China

E-mail: day1104241008@163.com (A.D.); wangtian_twang@163.com (T.W.); 7213007016@stu.jiangnan.edu.cn (S.W.); jchbob@163.com (C.J.); 1091200423@jiangnan.edu.cn (Q.M.); flhuang@jiangnan.edu.cn (F.H.)

* Corresponding Authors:

Fenglin Huang, flhuang@jiangnan.edu.cn

References

1. Bai, B.Y., Li, J.H., 2014. Positive Effects of K^+ Ions on Three-Dimensional Mesoporous Ag/Co_3O_4 Catalyst for HCHO Oxidation. ACS Catal. 4(8), 2753-2762. https://doi.org/10.1021/cs5006663
2. Bellat, J.P., Bezverkhyy, I., Weber, G., Royer, S., Averlant, R., Giraudon, J.M., Lamonier, J.F., 2015. Capture of formaldehyde by adsorption on nanoporous materials. J. Hazard Mater. 300, 711-717. https://doi.org/10.1016/j.jhazmat.2015.07.078
3. Bu, Y.B., Chen, Y.F., Jiang, G.M., Hou, X.M., Li, SM, Zhang, Z.T., 2020. Understanding of Au-CeO_2 interface and its role in catalytic oxidation of formaldehyde. Appl. Catal. B Environ. 260, 118138. https://doi.org/10.1016/j.apcatb.2019.118138
4. Cwele, T., Mahadevaiah, N., Singh, S., Friedrich, H.B., 2016. Effect of Cu additives on the performance of a cobalt substituted ceria ($Ce_{0.90}Co_{0.10}O_{2-\delta}$) catalyst in total and preferential CO oxidation. Appl. Catal. B Environ. 182, 1-14. https://doi.org/10.1016/j.apcatb.2015.08.043
5. Ding, J.Y., Liu, J., Yang, Y.J., Zhao, L.M., Yu, Y.N., 2022. Understanding A-site tuning effect on formaldehyde catalytic oxidation over La-Mn perovskite catalysts. J. Hazard. Mater. 422, 126931. https://doi.org/10.1016/j.jhazmat.2021.126931
6. Freyschlag, C.G., Madix, R.J, 2011. Precious metal magic: catalytic wizardry. Mater. Today 14(4), 134-142. https://doi.org/10.1016/S1369-7021(11)70085-2
7. Guo, Y.D., Di, Z.Y., Guo, X.N., Wei, Y., Zhang, R.D., Jia, J.B., 2023. N/Ce doped graphene supported Pt nanoparticles for the catalytic oxidation of formaldehyde at room temperature. J. Environ. Sci. 125, 135-147. https://doi.org/10.1016/j.jes.2021.12.033
8. He, M.M., Liu, X-Q., Li, M.J., Yang, Y., Chen, Z.Q., Jiang, W.D., Tang, H.M., Raymond, O., 2022. Multiple hydrogen bonds enhancing formaldehyde adsorption on functionalized zigzag graphene nanoribbons. Appl. Surf. Sci. 586, 152834. https://doi.org/10.1016/j.apsusc.2022.152834
9. Huang, F.L., Xu, Y.F., Peng, B., Su, Y.F., Jiang F., Hiesh, Y.L., Wei, Q.F., 2015. Coaxial Electrospun Cellulose-Core Fluoropolymer-Shell Fibrous Membrane from Recycled Cigarette Filter as Separator for High Performance Lithium-Ion Battery. ACS Sustain. Chem. Eng. 3(5), 932-940. https://doi.org/10.1021/acssuschemeng.5b00032
10. Huang, Y.C., Ye, K.H., Li, H.B., Fan, W.J., Zhao, F.Y., Zhang, Y.M., Ji, H.B., 2016. A highly durable catalyst based on $Co_xMn_{3-x}O_4$ nanosheets for low-temperature formaldehyde oxidation. Nano Res. 9(12), 3881-3892. https://doi.org/10.1007/s12274-016-1257-9

11. Ji, J., Lu, X.L., Chen, C., He, M., Huang, H.B., 2020. Potassium-modulated δ-MnO_2 as robust catalysts for formaldehyde oxidation at room temperature. Appl. Catal. BEnviron. 260, 118210. https://doi.org/10.1016/j.apcatb.2019.118210
12. Jia, J.B., Zhang, P.Y., Chen, L., 2016. Catalytic decomposition of gaseous ozone over manganese dioxides with different crystal structures. Appl. Catal. B Environ. 189, 210-218. https://doi.org/10.1016/j.apcatb.2016.02.055
13. Li, J.J., Hu, R.S., Zhang, J.G., Meng, W.W., Du, Y.F., Si, Y.F., Zhang, Z., 2016. Influence of preparation methods of La_2CoMnO_6/CeO_2 on the methane catalytic combustion. Fuel 178, 148-154. https://doi.org/10.1016/j.fuel.2016.03.041
14. Li, J.W., Pan, K.L., Yu, S.J., Yan, S.Y., Chang, M.B., 2014. Removal of formaldehyde over $Mn_xCe_{1-x}O_2$ catalysts: thermal catalytic oxidation versus ozone catalytic oxidation. J. Environ. Sci. 26(12), 2546-2553. https://doi.org/10.1016/j.jes.2014.05.030
15. Liang, X.J., Zhang, J.X., Song, W.L., Wang, K.W., Zhang, B.Y., 2018. Formaldehyde Exposure in Indoor Air From Public Places and Its Associated Health Risks in Kunshan City, China. Asia Pac. J. Public Health 30(6), 551-560. https://dx.doi.org/10.1177/1010539518800348
16. Liu, R.F., Li, W.B., Peng, A.Y., 2018. A facile preparation of TiO_2/ACF with C-Ti bond and abundant hydroxyls and its enhanced photocatalytic activity for formaldehyde removal. Appl. Surf. Sci. 427, 608-616. https://doi.org/10.1016/j.apsusc.2017.07.209
17. Liu, Y.S., Jiang, H., Hao, J.Y., Liu, Y.L., Shen, H.B., Li, W.Z., Li, J., 2017. Metal-Organic Framework-Derived Reduced Graphene Oxide-Supported ZnO/$ZnCo_2O_4$/C Hollow Nanocages as Cathode Catalysts for Aluminum-O_2 Batteries. ACS Appl. Mater. Interfaces 9(37), 31841-31852. https://doi.org/10.1021/acsami.7b08647
18. Liu, Y.F., Ye, C.C., Zhao, S-N., Wu, Y.Y., Liu, C., Huang, J.F., Xue, L., Sun, J.W., Zhang, W.Q., Wang, X., Xiong, P., Zhu, J.W., 2022. A dual-site doping strategy for developing efficient perovskite oxide electrocatalysts towards oxygen evolution reaction. Nano Energy 99, 107344. https://doi.org/10.1016/j.nanoen.2022.107344
19. Liu, Z.Y., Niu, J.P., Long, W.M., Cui, B., Song, K., Dong, F., Xu, D., 2020. Highly Efficient MnO_2/AlOOH Composite Catalyst for Indoor Low-Concentration Formaldehyde Removal at Room Temperature. Inorg. Chem. 59(10), 7335-7343. https://doi.org/10.1021/acs.inorgchem.0c00852
20. López-Suárez, F.E., Bueno-López, A., Illán-Gómez, M.J., Trawczynski, J., 2014. Potassium-copper perovskite catalysts for mild temperature diesel soot combustion. Appl. Catal. A-Gen. 485, 214-221. https://doi.org/10.1016/j.apcata.2014.07.037
21. Ma, C.Y., Yang, C.G., Wang, B., Chen, C., Wang, F.B., Yao, X.L., Song, M.Y., 2019. Effects of H_2O on HCHO and CO oxidation at room-temperature catalyzed by MCo_2O_4 (M=Mn, Ce and Cu) materials. Appl. Catal. B Environ. 254, 76-85. https://doi.org/10.1016/j.apcatb.2019.04.085
22. Ma, Q.P., Zhang, Y.Y., Zhu, X.Y., Chen, B.L., 2022. Hollow multi-shelled Co_3O_4 as nanoreactors to activate peroxymonosulfate for highly effective degradation of Carbamazepine: A novel strategy to reduce nano-catalyst agglomeration. J. Hazard Mater. 427, 127890. https://doi.org/10.1016/j.jhazmat.2021.127890
23. Mai, Z.H., Fan, S.Q., Wang, Y.L., Chen, J.J., Chen, Y., Bai, K., Deng, L., Xiao, Z.Y., 2022. Catalytic nanofiber composite membrane by combining electrospinning precursor seeding and flowing synthesis for immobilizing ZIF-8 derived Ag nanoparticles. J. Membrane Sci. 643, 120045. https://doi.org/10.1016/j.memsci.2021.120045
24. Mathew, T., Suzuki, K., Ikuta, Y., Takahashi, N., Shinjoh, H., 2012. Mesoporous ferrihydrite with incorporated manganese for rapid removal of organic contaminants in air. Chem. Commun. 48(89), 10987-10989. https://doi.org/10.1039/C2CC36120E
25. Meng, D.M., Xu, Q., Jiao, Y.L., Guo, Y, Guo, Y.L., Wang, L., Lu, G.Z., Zhan, W.C., 2018. Spinel structured $Co_aMn_bO_x$ mixed oxide catalyst for the selective catalytic reduction of NO_x with NH_3. Appl. Catal. B Environ. 221, 652-663. https://doi.org/10.1016/j.apcatb.2017.09.034

26. Morales, M., Espiell, F., Segarra, M., 2014. Performance and stability of $La_{0.5}Sr_{0.5}CoO_{3-\delta}$ perovskite as catalyst precursor for syngas production by partial oxidation of methane. Int. J. Hydrogen Energ. 39(12), 6454-6461. https://doi.org/10.1016/j.ijhydene.2014.02.060
27. Naragund, V.S., Panda, P.K., 2020. Electrospinning of cellulose acetate nanofiber membrane using methyl ethyl ketone and N, N-Dimethylacetamide as solvents. Mater. Chem. Phys. 240, 122147. https://doi.org/10.1016/j.matchemphys.2019.122147
28. Niu, M.S., Yang, H.H., Zhou, H., Yi, X.L., Zhou, X., Zhan, J.J., Liu, Y., 2022. Synergy of the successive modification of cryptomelane MnO_2 by potassium insertion and nitrogen doping for catalytic formaldehyde oxidation. Chem. Eng. J. 431, 133928. https://doi.org/10.1016/j.cej.2021.133928
29. Olaru, N., Andriescu, A., Olaru, L., 2001. On the hydrolysis of cellulose acetate in toluene/acetic acid/water system. Eur. Polym. J. 37(4), 865-867. https://doi.org/10.1016/S0014-3057(00)00183-X
30. Pereira, A.G.B., Fajardo, A.R., Gerola, A.P., Rodrigues, J.H.S., Nakamura, C.V., Muniz, E.C., Hsieh, Y.L., 2020. First report of electrospun cellulose acetate nanofibers mats with chitin and chitosan nanowhiskers: Fabrication, characterization, and antibacterial activity. Carbohydr Polym. 250, 116954. https://doi.org/10.1016/j.carbpol.2020.116954
31. Phan, D.N., Lee, H., Huang, B., Mukai, Y., Kim, I.S., 2018. Fabrication of electrospun chitosan/cellulose nanofibers having adsorption property with enhanced mechanical property. Cellulose 26(3), 1781-1793. doi: 10.1007/s10570-018-2169-5
32. Qu, F.D., Thomas, T.J., Zhang, B.X., Zhou, X.X., Zhang, S.D., Ruan, S.P., Yang, M.H., 2018. Self-sacrificing templated formation of $Co_3O_4/ZnCo_2O_4$ composite hollow nanostructures for highly sensitive detecting acetone vapor. Sensor Actuat. B Chem. 273, 1202-1210. https://doi.org/10.1016/j.snb.2018.07.005
33. Silva, R.X., de Menezes, A.S., Almeida, R.M., Moreira, R.L., Paniago R., Marti X., Reichlova, H., Maryško, M., Rezende, M.V.D., Paschoal, C.W.A., 2016. Structural order, magnetic and intrinsic dielectric properties of magnetoelectric La_2CoMnO_6. J. Alloy. Compd. 661, 541-552. https://doi.org/10.1016/j.jallcom.2015.11.097
34. Tang, X.J., Bai, Y., Duong, A., Smith, M.T., Li, L.Y., Zhang, L.P., 2009. Formaldehyde in China: production, consumption, exposure levels, and health effects. Environ. Int. 35(8), 1210-1224. https://doi.org/10.1016/j.envint.2009.06.002
35. Tang, X.F., Li, Y.G., Huang, X.M., Xu, Y.D., Zhu, H.Q., Wang, J.G., Shen, W.J., 2006. MnO_x-CeO_2 mixed oxide catalysts for complete oxidation of formaldehyde: Effect of preparation method and calcination temperature. Appl. Catal. B Environ. 62(3-4), 265-273. https://doi.org/10.1016/j.apcatb.2005.08.004
36. Vikrant, K., Kim, K.H., Dong, F., Boukhvalov, D.W., Choi, W., 2022. Deep oxidation of gaseous formaldehyde at room-temperature by a durable catalyst formed through the controlled addition of potassium to platinum supported on waste eggshell. Chem. Eng. J. 428, 131177. https://doi.org/10.1016/j.cej.2021.131177
37. Wang, Q.Q., Ma, L, Wang, L.C., Wang, D.D., 2019. Mechanisms for enhanced catalytic performance for NO oxidation over La_2CoMnO_6 double perovskite by A-site or B-site doping: Effects of the B-site ionic magnetic moments. Chem. Eng. J. 372, 728-741. https://doi.org/10.1016/j.cej.2019.04.178
38. Wu, S.L., Shi, J.Y., Nie, X.L., Yao, Y.M., Jiang, F., Wei, Q.F., Huang, F.L., 2022. Microporous Cyclodextrin Film with Funnel-type Channel Polymerized on Electrospun Cellulose Acetate Membrane as Separators for Strong Trapping Polysulfides and Boosting Charging in Lithium-Sulfur Batteries. Energy Environ. Mater. Online. https://dx.doi.org/10.1002/eem2.12319
39. Xu, Y., Dhainaut, J., Dacquin, J.P., Mamede, A.S., Marinova, M., Lamonier, J.F., Vezin, H., Zhang, H., Royer, S., 2021. $La_{1-x}(Sr, Na, K)_xMnO_3$ perovskites for HCHO oxidation: The role of oxygen species on the catalytic mechanism. Appl. Catal. B Environ. 287, 119955. https://doi.org/10.1016/j.apcatb.2021.119955
40. Yang, L., Li, Y.Z., Sun, Y.D., Wang, W., Shao, Z.P., 2022. Perovskite Oxides in Catalytic Combustion of Volatile Organic Compounds: Recent Advances and Future Prospects. Energy Environ. Mater. Online. https://dx.doi.org/10.1002/eem2.12256

41. Ye, J.W., Yu, Y., Fan, J.J., Cheng, B., Yu, J.G., Ho, W.K., 2020. Room-temperature formaldehyde catalytic decomposition. Environ. Sci. Nano 7(12), 3655-3709. https://dx.doi.org/10.1039/d0en00831a
42. Yusuf, A., Sun, Y., Snape, C., He, J., Wang, C.J., Ren, Y., Jia, H.P., 2020. Low-temperature formaldehyde oxidation over manganese oxide catalysts: Potassium mediated lattice oxygen mobility. Mol. Catal. 497, 111204. https://doi.org/10.1016/j.mcat.2020.111204
43. Zhang, K., Li, Z.J., Kang, W.M., Deng, N.P., Yan, J., Ju, J.G., Liu, Y., Cheng, B.W., 2018. Preparation and characterization of tree-like cellulose nanofiber membranes via the electrospinning method. Carbohydr. Polym. 183, 62-69. https://doi.org/10.1016/j.carbpol.2017.11.032
44. Zhang, L., Shi, L.Y., Huang, L., Zhang, J.P., Gao, R.H., Zhang, D.S., 2014. Rational Design of High-Performance DeNO$_x$ Catalysts Based on $Mn_xCo_{3-x}O_4$ Nanocages Derived from Metal-Organic Frameworks. ACS Catal. 4(6), 1753-1763. https://dx.doi.org/10.1021/cs401185c
45. Zhang, W.B., Yang, K.Y., Han, X.S., Cai, H.Z., Lu, W.Y., Yuan, Y.H., Zhang, S.Y., Gao, F., 2022. Metal-organic frameworks decorated pomelo peel cellulose nanofibers membranes for high performance dye rejection. Colloid Surface A. 649, 129393. https://doi.org/10.1016/j.colsurfa.2022.129393
46. Zhao, X.W., Zhang, Z.Y., Song, N., Shi, J.L., Yang, N., Nie, G.D., Wang, C., 2021. Vanadium/cobalt oxides-anchored flexible carbon nanofibers with tunable magnetism as recoverable peroxidase-like catalysts. Mater. Today Chem. 22, 100568. https://doi.org/10.1016/j.mtchem.2021.100568
47. Zhou, T., Zhao, L., Wu, D.S., Feng, Q., Zhao, B.B., 2022. Uniformly assembled polypyrrole-covered bacterial cellulose/g-C_3N_4 flexible nanofiber membrane for catalytic degradation of tetracycline hydrochloride. J. Water. Process Eng. 47, 102775. https://doi.org/10.1016/j.jwpe.2022.102775

Figures

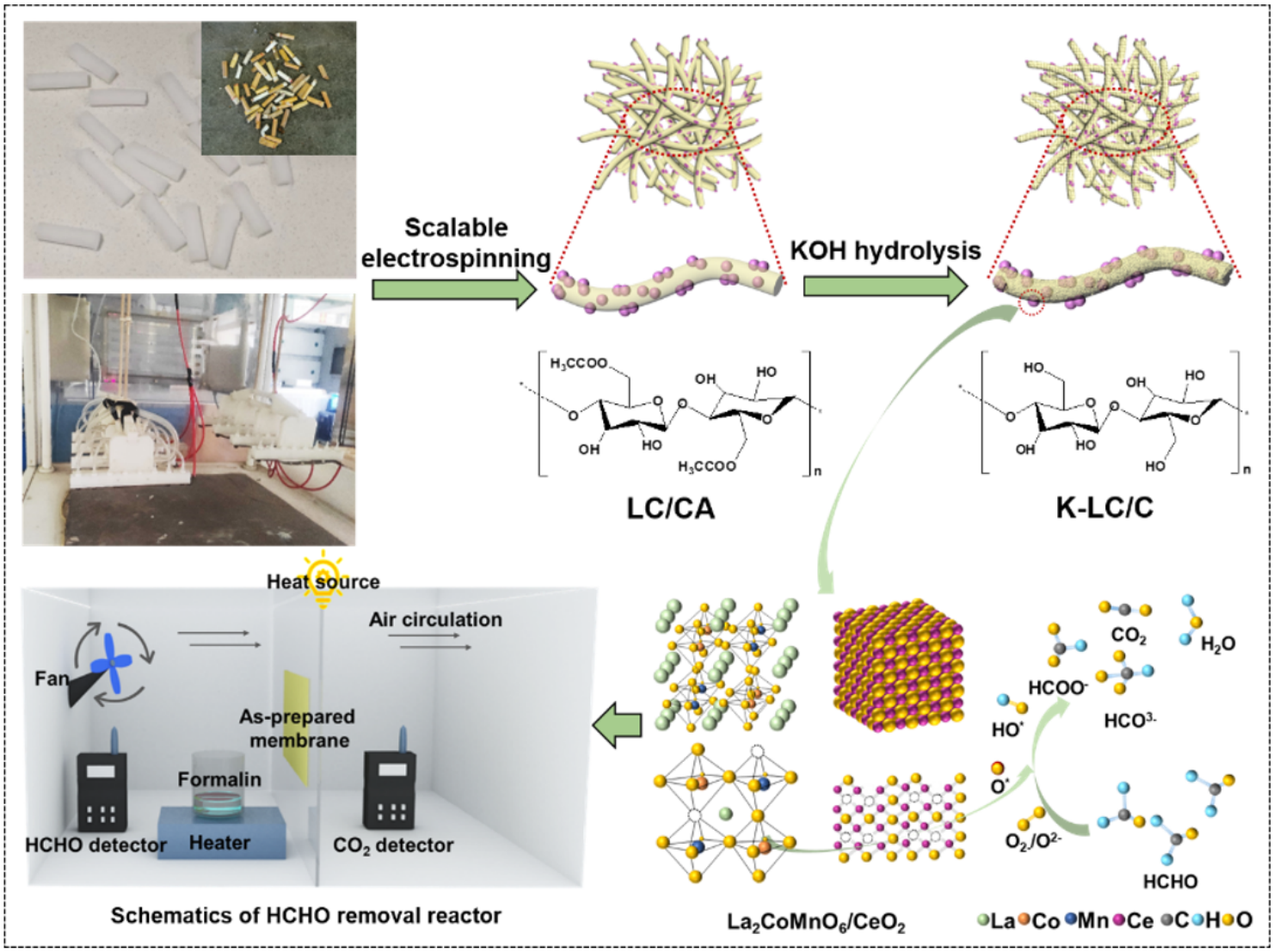

Figure 1

Scalable fabrication of the K-LC/C nanofibrous membrane and schematic diagram for formaldehyde removal

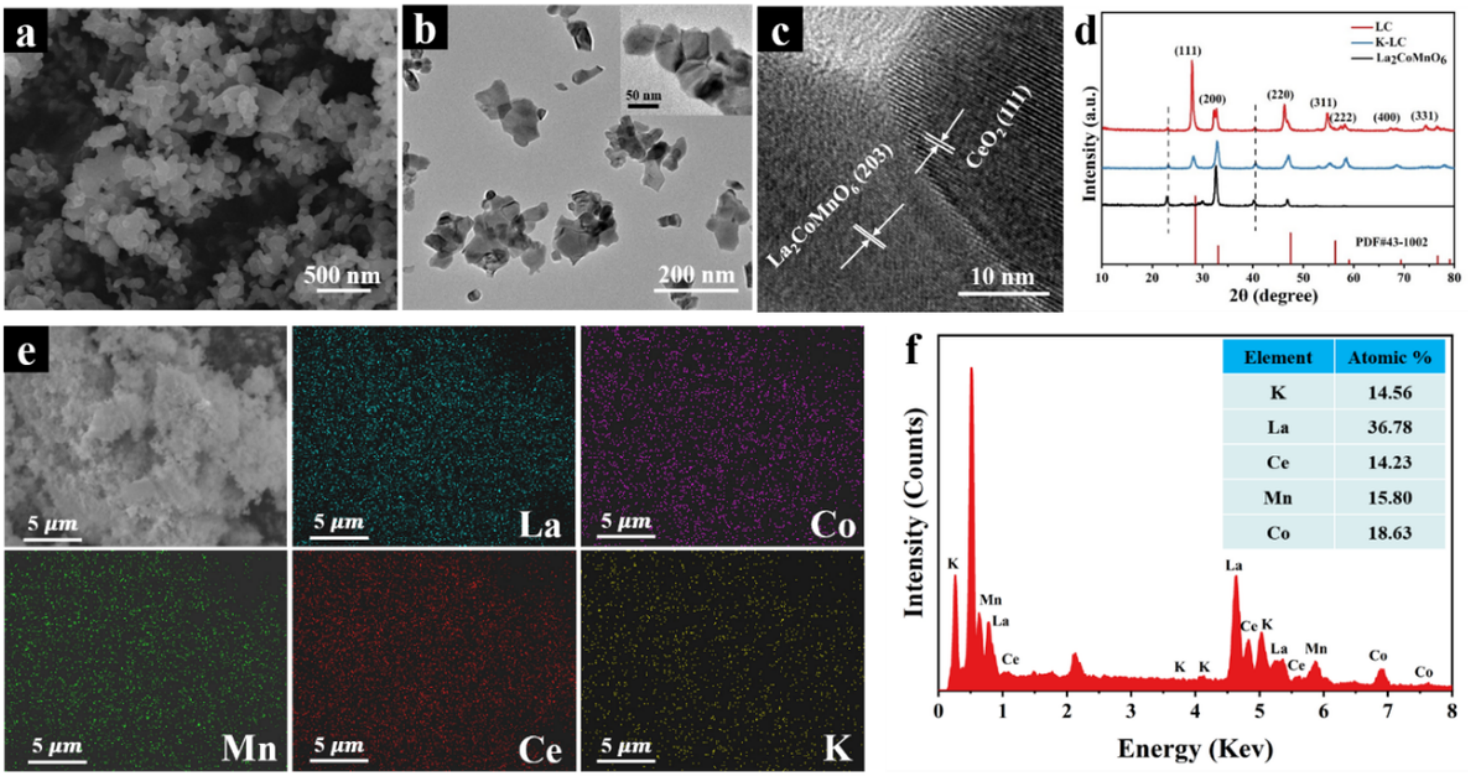

Figure 2

(a) SEM, (b) TEM and (c) HTTEM images of LC (the inset shows the corresponding high magnification TEM image). (d) XRD patterns of LC, K-LC and La2CoMnO6. (e) EDS-Mapping images of the elements and (f) EDS pattern collected from the K-LC.

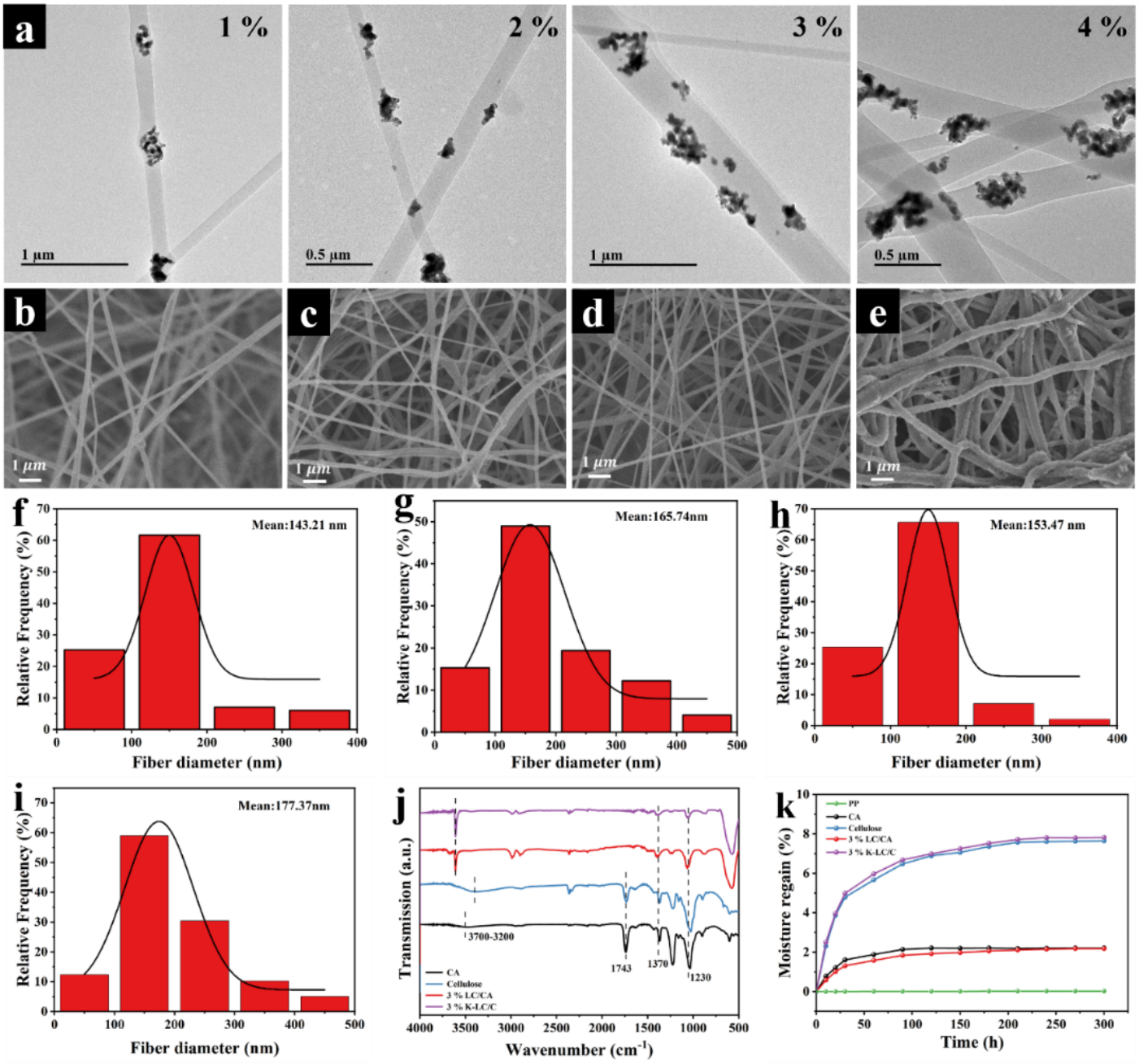

Figure 3

(a) TEM images of 1%, 2%, 3% and 4% LC/CA nanofibrous membrane. SEM images of CA (b), cellulose (c), 3 % LC/CA (d) and 3 % K-LC/C (e) nanofibrous membrane (the inset showed corresponding fiber diameter distribution images). (f) FTIR spectra and (g) Moisture absorption curve of CA, cellulose, 3 % LC/CA and 3 % K-LC/C nanofibrous membrane.

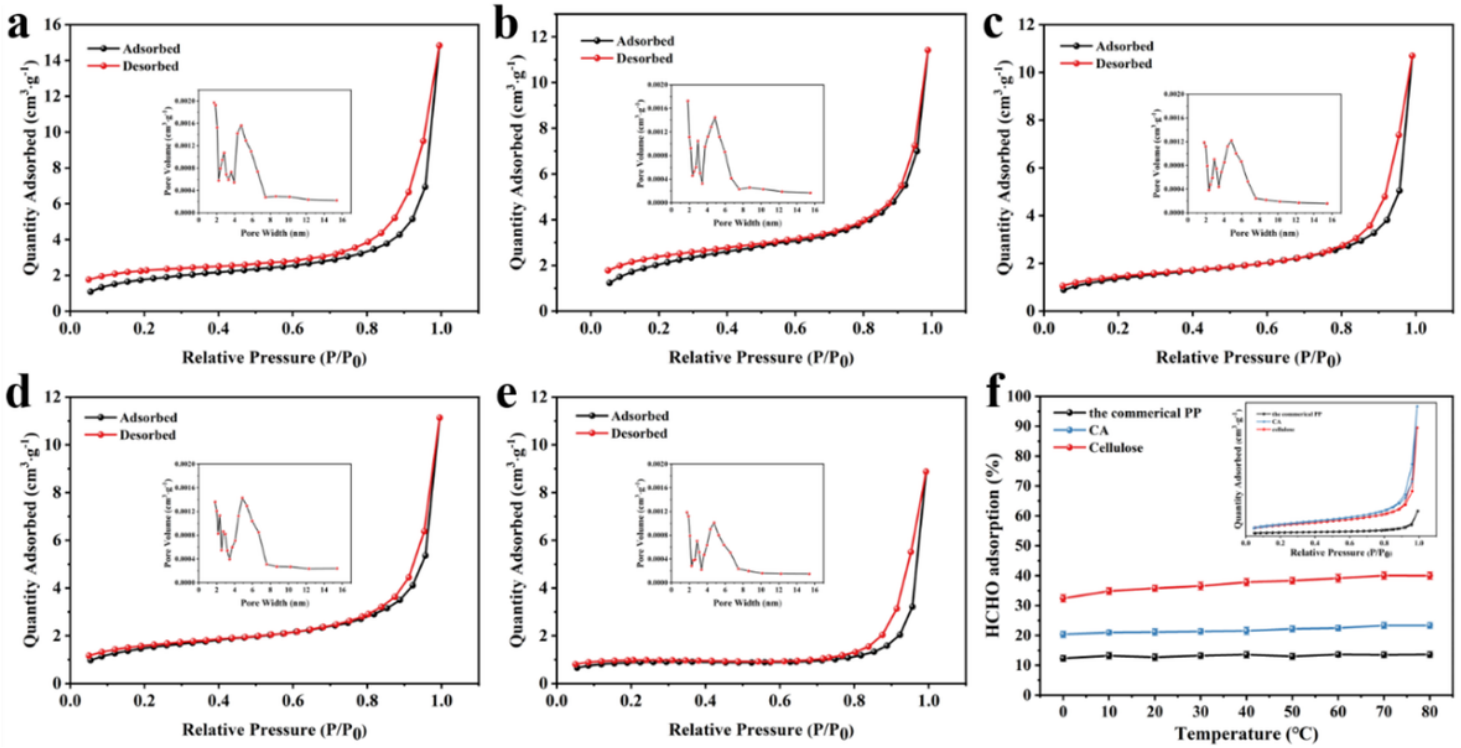

Figure 4

N2adsorption-desorption isotherms measured for cellulose (a), 1 % (b), 2 % (c), 3 % (d) and 4 % (e) K-LC/C nanofibrous membrane, and the inset shows the corresponding pore size distribution curves. (f) Formaldehyde adsorption efficiency of the commercial PP, CA and cellulose nanofibrous membrane (the inset shows the corresponding N2 adsorption-desorption isotherms).

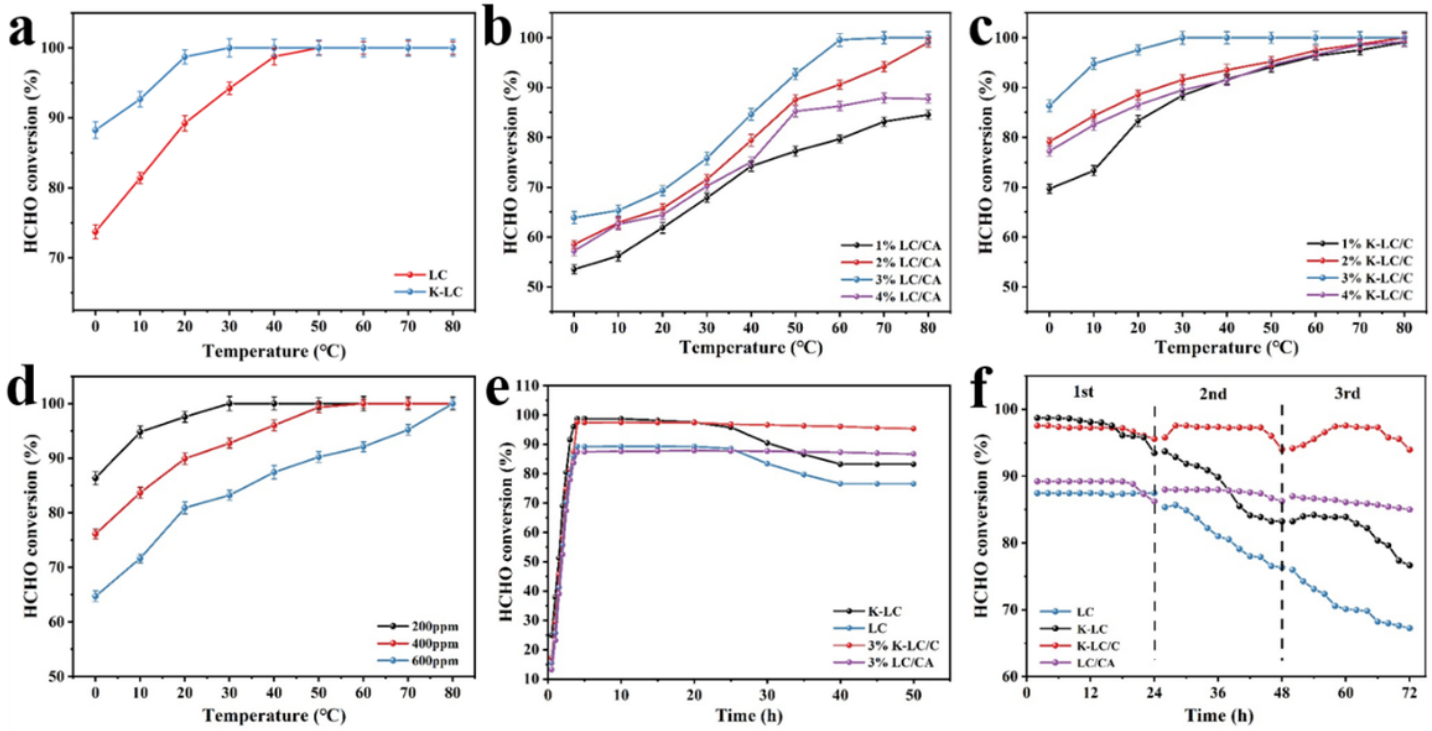

Figure 5

(a) Formaldehyde conversion of LC and K-LC NPs. Formaldehyde conversion of LC/CA (b) and K-LC/C (c) nanofibrous membrane with different concentrations. (d) Effect of 3 % K-LC/C membrane on HCHO conversion with different initial concentration. (e) Curve of the HCHO conversation overtime in different sample. (f) Catalytic stability of different sample in HCHO oxidation.

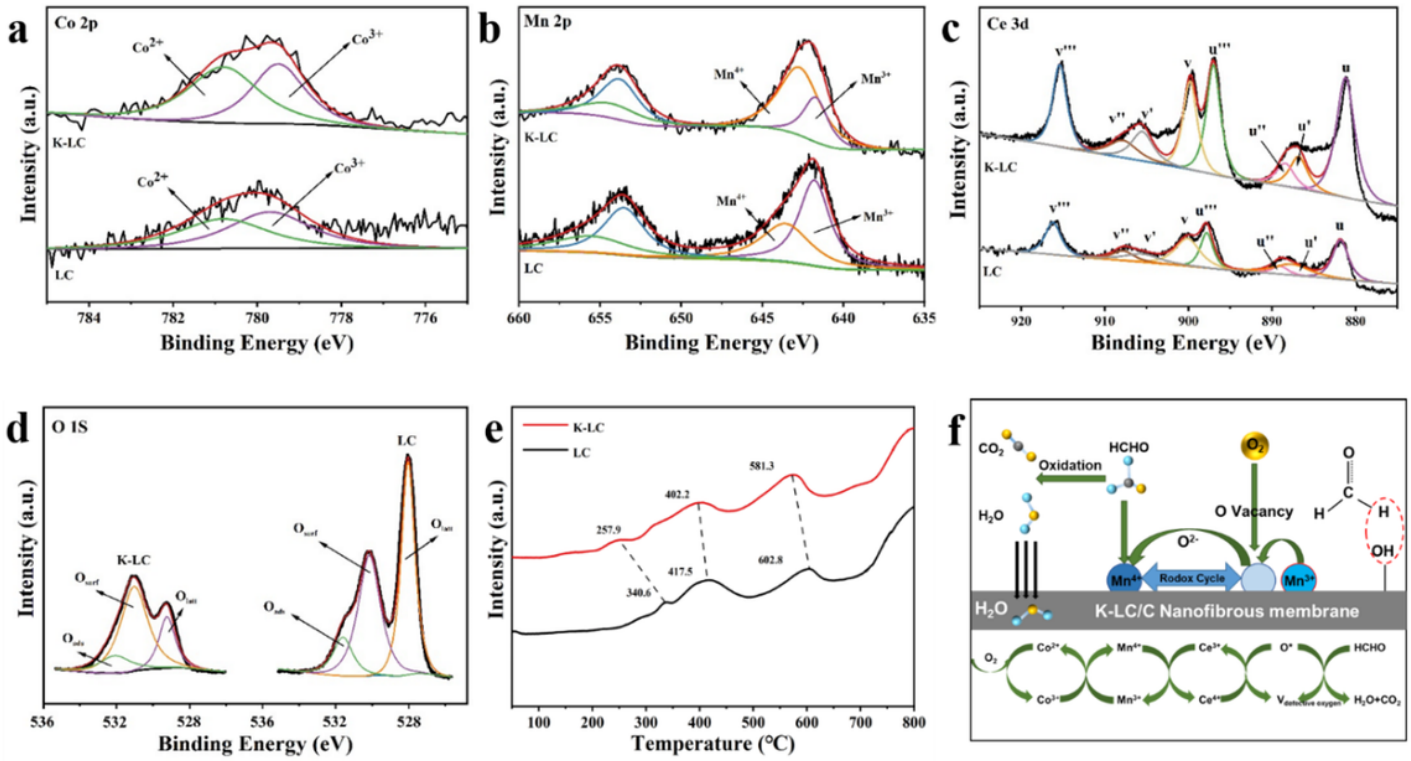

Figure 6

XPS spectra for Co 2p (a), Mn 2p (b), Ce 3d (c) and O 1s (d) of the LC and K-LC NPs. (e) H2-TPR profiles of the LC and K-LC NPs. (f) The proposed pathway of formaldehyde catalytic oxidation over K-LC/C nanofibrous membrane.